25113 and probe 2 corresponds to nucleotides 78807 through 79341 of BAC clone RPCI11-388A16.
13. Primers near deletion endpoints were used to direct PCR with genomic DNA from kindred members as template (Web table 2) (*21*). Products were fractionated by agarose gel electrophoresis and subjected to DNA sequencing.
14. F. H. Wilson *et al.*, data not shown.
15. The genomic and mRNA structure of *hWNK1* and *hWNK4* was determined by genomic and EST database mining with experimental confirmation (*21*). The cDNA sequence of *hWNK1* has recently been independently submitted to GenBank (NM_018979). The cDNA sequence of *hWNK4* has been deposited in GenBank (AF390018) (Web fig. 1) (*21*).
16. B. Xu *et al.*, *J. Biol. Chem.* **275**, 16795 (2000).
17. Probes spanning exons 5 through 8 of *hWNK1* or exons 16 through 19 of *hWNK4* were hybridized to human multiple-tissue Northern blots (Clontech). Independent blots yield comparable results.
18. Other deletions in intron 1 were sought in unaffected subjects by quantitative PCR and Southern blotting; no deletions that overlap those found in K22 and K4 were identified, although a more proximal 8-kb deletion, unrelated to PHAII, was found to have an allele frequency of 10% in caucasians (*21*).
19. Variants in *WNK1* and *WNK4* were sought using single-strand conformational polymorphism analysis with specific primer pairs (Web table 3) (*21*) directing PCR using genomic DNA as a template. The DNA sequence of identified variants was determined.
20. Levels of gene transcripts were evaluated by real-time quantitative reverse transcription PCR (RT-PCR) using RNA extracted from leukocytes of members of K4 and control subjects (*21*).
21. Supplementary data are available at www.sciencemag.org/cgi/content/full/293/5532/1107/DC1.
22. For *WNK1*, rat sequence is known (*16*) and for *WNK4*, mouse (F. Wilson, unpublished data) and rat sequence (H. Toka, unpublished data) are known from genomic mining and PCR amplification of kidney cDNA.
23. Z. Farfel *et al.*, *Arch. Intern. Med.* **138**, 1828 (1978).
24. Kindred 13 was as previously described with an additional six members characterized since the initial linkage report (*7*); analysis of linkage in the extended kindred yielded a lod score of 5.4, localizing the disease gene to a 16-cM interval flanked by loci *D17S1166* and *D17S931*.
25. The index case of K23 has hypertension, hyperkalemia, distal renal tubular acidosis, suppressed plasma renin activity, and normal glomerular filtration, typical of PHAII.
26. M. R. Lee, S. G. Ball, T. H. Thomas, D. B. Morgan, *Q. J. Med.* **48**, 245 (1979).
27. M. R. Lee, D. B. Morgan, *Lancet* **1**, 879 (1980).
28. M. Baz *et al.*, *Presse Med.* **19**, 1981 (1990).
29. Affinity-purified antibodies to WNK1 and WNK4 were prepared (*21*). Their specificities were established by immunoblotting, demonstrating staining of the immunizing peptide and proteins of appropriate size in mouse kidney (*21*). All staining was competed by the immunizing peptide (*14*).
30. Sections (3 μm thickness) were cut from frozen mouse kidney specimens, fixed, immunostained with indicated antibodies, and subjected to immunofluorescence microscopy. WNK1 and WNK4 staining were both competed by the immunizing peptide (*14*).
31. J. L. Madara, *Annu. Rev. Physiol.* **60**, 143 (1998).
32. D. B. Simon *et al.*, *Science* **285**, 103 (1999).
33. V. L. Schuster, J. B. Stokes, *Am. J. Physiol.* **253**, F203 (1987).
34. D. Levy *et al.*, *Hypertension* **36**, 477 (2000).
35. C. Julier *et al.*, *Hum. Mol. Genet.* **6**, 2077 (1997).
36. J. Baima *et al.*, *Hypertension* **34**, 4 (1999).
37. G. M. Lathrop *et al.*, *Proc. Natl. Acad. Sci. U.S.A.* **81**, 3443 (1984).
38. The left and right ends of the segment shown lie at nucleotide positions 9575 and 107547 on BAC clone accession AC004765 in GenBank.
39. A. Lupas, M. Van Dyke, J. Stock, *Science* **252**, 1162 (1991).
40. Amino acids for WNK2 and WNK3 are numbered with respect to GenBank entries reporting partial sequence for these genes (hWNK2, GenBank accession AB044546; hWNK3, GenBank accession AJ409088).
41. We thank the families studied for their invaluable contribution to this work. Supported in part by an NIH Specialized Center of Research in Hypertension, grants from INSERM and the Association Claude Bernard. S.D-N. is a fellow of the Ministère de l'Education Nationale, de la Recherche et de la Technologie. K.C. is an investigator of the Medical Scientist Training Program. RPL is an investigator of the Howard Hughes Medical Institute.

24 May 2001; accepted 29 June 2001

REPORTS

Resolving the Structure of Ionized Helium in the Intergalactic Medium with the Far Ultraviolet Spectroscopic Explorer

G. A. Kriss,[1,2]* J. M. Shull,[3] W. Oegerle,[4] W. Zheng,[2] A. F. Davidsen,[2]† A. Songaila,[5] J. Tumlinson,[3] L. L. Cowie,[5] J.-M. Deharveng,[6] S. D. Friedman,[2] M. L. Giroux,[3] R. F. Green,[7] J. B. Hutchings,[8] E. B. Jenkins,[9] J. W. Kruk,[2] H. W. Moos,[2] D. C. Morton,[8] K. R. Sembach,[2] T. M. Tripp[9]

The neutral hydrogen (H I) and ionized helium (He II) absorption in the spectra of quasars are unique probes of structure in the early universe. We present Far-Ultraviolet Spectroscopic Explorer observations of the line of sight to the quasar HE2347-4342 in the 1000 to 1187 angstrom band at a resolving power of 15,000. We resolve the He II Lyman α (Lyα) absorption as a discrete forest of absorption lines in the redshift range 2.3 to 2.7. About 50 percent of these features have H I counterparts with column densities $N_{H\ I} > 10^{12.3}$ per square centimeter that account for most of the observed opacity in He II Lyα. The He II to H I column density ratio ranges from 1 to >1000, with an average of ~80. Ratios of <100 are consistent with photoionization of the absorbing gas by a hard ionizing spectrum resulting from the integrated light of quasars, but ratios of >100 in many locations indicate additional contributions from starburst galaxies or heavily filtered quasar radiation. The presence of He II Lyα absorbers with no H I counterparts indicates that structure is present even in low-density regions, consistent with theoretical predictions of structure formation through gravitational instability.

The intergalactic medium (IGM) is the gaseous reservoir that provides the raw material for the galaxies that dominate our view of the visible universe. By observing distant bright objects such as quasars, we can explore the IGM by examining the absorption features it imprints on the transmitted light. These absorption features trace structure in the universe at epochs intermediate between the earliest density fluctuations seen in the cosmic background radiation and the distribution of galaxies visible today. The distribution of absorption features according to redshift (z) and the column densities of gaseous material in different ions reveal the structure of the IGM and its density and ionization state. From the ionization state of the gaseous species, we can also infer the processes responsible for ionizing the gas (e.g., radiation from quasars in the early universe or from early bursts of star formation).

The lack of smooth Lyα absorption by H

[1]Space Telescope Science Institute, 3700 San Martin Drive, Baltimore, MD 21218, USA. [2]Center for Astrophysical Sciences, Department of Physics and Astronomy, Johns Hopkins University, Baltimore, MD 21218, USA. [3]CASA and JILA, Department of Astrophysical and Planetary Sciences, University of Colorado, Campus Box 389, Boulder, CO 80309, USA. [4]Laboratory for Astronomy and Solar Physics, Code 681, NASA/Goddard Space Flight Center, Greenbelt, MD 20771, USA. [5]Institute for Astronomy, University of Hawaii, 2680 Woodlawn Road, Honolulu, HI 96822, USA. [6]Laboratorie d'Astronomie Spatiale, BP 8, 13376 Marseille Cedex 12, France. [7]Kitt Peak National Observatory, National Optical Astronomy Observatories, Post Office Box 26732, 950 North Cherry Avenue, Tucson, AZ 85726, USA. [8]Herzberg Institute of Astrophysics, National Research Council of Canada, Victoria, BC V8X 4M6, Canada. [9]Princeton University Observatory, Princeton, NJ 08544, USA.

*To whom correspondence should be addressed. E-mail: gak@stsci.edu
†Deceased.

I in quasar spectra (*1*) led to the conclusion that any diffusely distributed gas must be too highly ionized to be visible. Discrete absorption features were so plentiful, however, that they were dubbed the "Lyman α forest" (*2*). Because ionized helium (He^+) is more difficult to ionize than hydrogen (ionization potential of 54.4 eV versus 13.6 eV) and recombines faster, its abundance in the IGM is expected to be higher. Searches for a diffuse component of the IGM therefore concentrated on absorption from He II Lyα λ304 Å (*3*). This absorption was first observed using the Hubble Space Telescope (HST) (*4*) along the line of sight to the quasar Q0302-003 (z = 3.29). The observation showed the IGM to be essentially opaque at redshifts of $z \sim 3$, and it seemed possible that the material in the H I Lyα forest was sufficient to account for the He II opacity (*5*). However, because no discrete He II features could be observed, this required several assumptions. Measurement (*6*) of the He^+ opacity at lower z, using the Hopkins Ultraviolet Telescope (HUT), showed a translucent medium with He II optical depth $\tau \sim 1$ at $z \sim 2.4$. The HUT observations were of insufficient spectral resolution to detect discrete He II absorption features. However, models of the sight line toward the quasar HS1700+64 (z = 2.72) required a substantial contribution to the He II opacity from He^+ that was more smoothly distributed than the known H I Lyα absorbers (*6, 7*), and improved HST observations of Q0302-003 also required more He II opacity than that predicted by the H I absorption (*8*). Resolution of these inconsistencies requires observations at higher spectral resolution.

Recent theoretical studies view the high-redshift IGM as a tracer of cosmic structure formation by gravitational instability. In such a scenario, diffusely distributed baryonic material (the protons and neutrons that constitute ordinary matter) responds to the gravitational influence of the underlying dark matter. The most overdense regions collapse first to form the earliest galaxies. This leaves the remaining gas as the IGM. Rather than being a uniform medium filling the space between galaxies, the IGM itself should show structure on scales larger than that of individual galaxies. Both numerical calculations (*9–16*) and analytic theory (*17–21*) link the evolving structure of the IGM to the H I and He II absorption visible in the spectra of high-redshift quasars.

Given the unsettled observational issues and the need to test the theoretical expectations, we planned Far-Ultraviolet Spectroscopic Explorer (FUSE) observations of the He II absorption toward the bright (visual magnitude V = 16.1) z = 2.885 quasar HE2347-4342 at high spectral resolution. Previous observations of HE2347-4342 at longer ultraviolet (UV) wavelengths showed it to be one of the brightest candidates for such observations (*22, 23*). As with the other quasars observed with HST, the He II absorption in this object is mostly opaque, but there are wavelength intervals of high transmission that suggest we can see the beginnings of the He^+ reionization in the IGM in the redshift range accessible toward this quasar (*22*). Because He II Lyα at z = 2.885 is redshifted to 1181 Å and HST is sensitive only down to 1150 Å, which corresponds to z = 2.79, the HST data do not cover a large range in redshift. We therefore hoped to trace this reionization process over a greater range with FUSE because its short-wavelength sensitivity would let us probe the IGM to much lower redshifts, down to $z \sim 2.0$ in principle (*24*).

We observed HE2347-4342 with FUSE in two separate campaigns. The first observation, from 17 to 27 August 2000, comprised 351,672 s, of which 192,610 s was during orbital night (*25*). The second, running from 11 to 21 October 2000, accumulated 249,717 s, with 183,630 s during orbital night. For each observing campaign, HE2347-4342 was centered in the 30 arc sec × 30 arc sec apertures. To maintain the optical alignment of the four channels during these campaigns, we offset FUSE every other day to the nearby UV-bright star WD2331-475 and performed routine adjustments to the mirror positions.

At the faint flux levels presented by HE2347-4342 ($F_\lambda \sim 3 \times 10^{-15}$ erg cm^{-2} s^{-1} Å^{-1} at 1200 Å), an accurate extraction of a background-subtracted, calibrated source spectrum from the two-dimensional (2D) recorded data required customized processing. Because the LiF channels have a throughput that is ~3 times that of the SiC channels, we discuss only the LiF portions of the spectrum. Because there are spatial variations in the background that affect the extracted flux level in a source as faint as HE2347-4342, we turned off the standard background subtraction in the FUSE data-processing pipeline and extracted a "source + background" spectrum (*26*). We then manually extracted background spectra from the geometrically rectified detector images using regions lying adjacent to the source spectrum. Dead spots and airglow lines from other FUSE apertures were masked out of these background spectra. We computed a linear slope joining the two background regions, and scaled the final result for each of the four detector segments to match the level at the location of the extracted source + background spectrum. We subtracted these background spectra from the pipeline-extracted source + background spectra, and then used the rest of the normal pipeline processes to perform the standard wavelength and flux calibrations. At all steps we propagated a 1σ error array along with the data.

The multiplicity of detectors in FUSE and our two separate observations allowed several checks on our reduction process. At each wavelength we obtained two separate extracted spectra from each observation, for a total of four independent spectra. All spectral features noted in our combined spectrum were visible in each independent spectrum. As a check on our flux levels, we computed the scatter among the fluxes from the 1000 to 1080 Å spectra (2.7×10^{-16} erg cm^{-2} s^{-1} Å^{-1}) and the 1100 to 1187 Å spectra (2.1×10^{-16} erg cm^{-2} s^{-1} Å^{-1}). For both, the scatter is higher than our 1σ errors, indicating some residual systematic errors. These errors are ~5 to 10% of the extrapolated continuum flux for HE2347-4342, and they are indicative of our overall uncertainty. As a check on our zero levels, we note that the interstellar absorption line C II λ1036 is saturated in all FUSE extragalactic spectra. All four extracted spectra containing this line have zero flux at line center to within the 1σ error bars. At wavelengths of >1150 Å, previous HST observations of HE2347-4342 show several regions where there is little or no flux. Again, our extracted spectra also show no net flux in these regions to within our 1σ errors. Given the consistency among these separate observations, we combined the separate spectra into a single spectrum with a uniform wavelength scale and 0.05 Å bins (Fig. 1).

Because the FUSE bandpass stops short of wavelengths where the unobscured continuum of HE2347-4342 is visible (λ > 1190 Å), we obtained low-resolution HST spectra covering 1150 to 3200 Å on 21 August and 16 October 2000 to establish the continuum level. These observations each consisted of a 1060-s exposure using the Space Telescope Imaging Spectrograph (STIS) with grating G140L and a 600-s exposure using grating G230L. HE2347-4342 was slightly fainter (by 7%) in the October observation, but otherwise the spectra were identical. We scaled the October observation up to the August flux levels and fitted a simple power law, $F_\lambda = 3.31 \times 10^{-15}(\lambda/1000\ \text{Å})^{-2.40}$ erg cm^{-2} s^{-1} Å^{-1}, with an extinction correction to spectral regions free of galactic absorption lines. We used a mean galactic extinction curve with ratio of selective to total extinction $R_V = 3.1$ (*27*) and a color excess $E(B - V) = 0.014$ (*28*), where B is the blue-band magnitude.

The spectrum and extrapolated continuum (Fig. 1) shows that for $z > 2.72$ ($\lambda \gtrsim 1130$ Å), the IGM is relatively opaque, with occasional narrow windows that are nearly transparent (*22, 23*). At z = 2.72, the IGM becomes more transmissive, and the opacity systematically drops at lower z and shorter wavelengths. In this translucent region, it is also apparent that discrete absorption features account for most, if not all, of the opacity. We have resolved the He II absorption into a He II Lyα forest, analogous to the H I Lyα forest.

The quantitative character of the evolution in opacity with redshift is consistent with our expectations. The mean opacity over the redshift interval 2.3 to 2.7 is $\tau_{\mathrm{He\ II}} = 0.91 \pm 0.01$ (*29*), similar to the sight line toward HS1700+64 (*6*). We compare the measured opacities to a model (*21*) of discrete clouds photoionized by the general quasar population, valid for epochs after He II reionization is complete. In the model, ionization fluctuations on scales of ~4000 km s^{-1} (~15 Å, the size of our largest bins) lead to the predicted range of opacities (Fig. 2). For $z <$ 2.72, where He II reionization is potentially complete, the absolute level of the observed opacity, its trend to lower values at lower redshift, and the fluctuations about the mean are all consistent with this model.

The extrapolated STIS continuum is consistent with the peak fluxes in the FUSE spectrum (Fig. 1). Positive residuals from points above the extrapolated continuum have a Gaussian distribution consistent with the 1σ error bars on our data points, indicating that there are absorption-free windows where the IGM is transparent in He II Lyα. For models in which the physical density of smoothly distributed He II evolves as $n_{\mathrm{He\ II}} \propto (1+z)^{\alpha}$, and assuming a deceleration parameter $\Lambda = 0$ and density parameter $\Omega = 1$, the opacity in smoothly distributed He II Lyα varies with z as $\tau_{\mathrm{smooth}}(z) = \tau_{\mathrm{smooth}}(z = 2.885)[(1+z)/(1+2.885)]^{\alpha-1.5}$ for $z <$ 2.885 (*1*). By requiring that the distribution of the ratios of positive residuals to the 1σ errors be consistent with a Gaussian of mean 0 and dispersion 1, we set a 1σ upper limit on $\tau_{\mathrm{smooth}}(z = 2.885)$ by permitting $\tau_{\mathrm{smooth}}(z = 2.885)$, the power-law index, and its normalization to vary freely until χ^2 increases by 1. This yields an upper limit of $\tau_{\mathrm{smooth}}(z = 2.885) < 0.11$ to 0.12 for $\alpha = 0$ to 6.

Because the FUSE data resolve the He II Lyα forest, we can make a detailed comparison of the individual absorption features to their counterparts in the H I Lyα forest. To measure the individual He II column densities, we fit the FUSE spectrum using the program SPECFIT (*30*). Our model incorporates the extrapolated continuum, individual He II absorption lines with Voigt profiles (assuming Doppler widths of $b_{\mathrm{He\ II}} = b_{\mathrm{H\ I}}$), and foreground interstellar absorption in the Milky Way (*31*). For each He II line, we permit the column density to vary, but we fix z and the line width ($b_{\mathrm{He\ II}} = b_{\mathrm{H\ I}}$) to have the same values as those in the H I line list from a Keck observation of HE2347-4342 with a resolution of 8 km s^{-1} (*32*). The H I lines identified in the Keck spectrum (184 in total) all have He II counterparts (Fig. 3). Although these lines account for most of the observed opacity in He II Lyα, they account for only ~50% of the observed spectral features. To model the remaining features, we inserted additional lines whose redshifts were permitted to vary freely and whose widths were fixed at $b = 27$ km s^{-1}, the mean of the distribution from the H I line list. Over the 1000 to 1130 Å wavelength range, 179 additional He II Lyα absorption features were added to our fit. At the 3σ confidence limit, we are sensitive to He II lines with a limiting column density of log N(He II) $> 10^{12.8}$ cm^{-2}. For comparison, there are 72 H I Lyα features with $N_{\mathrm{H\ I}} < 10^{13}$ cm^{-2} in the same corresponding range in z in the Keck spectrum.

The added features are consistent with an extrapolation of the number of H I lines per unit column density of the form $f(N_{\mathrm{H\ I}}) \propto N_{\mathrm{H\ I}}{}^{-1.5}$ (*21, 33, 34*) down to column densities of ~10^{11} cm^{-2}. This is potentially a substantial amount of material, but, given the power-law form of the column density distribution, it does not dominate the total mass in the Lyα forest (*19*). Because the physical sizes of the absorbers and the ionization corrections are uncertain, we refrain from estimating the amount of mass that this population of absorbers represents. However, in the context of hydrodynamical models of the IGM (*14, 19*), we note that the low-column-density extension of the Lyα forest contains ~10% of the baryons at $z = 2$ to 3. Our detection of a large number of He II absorption features with no H I counterparts is consistent with the predictions of these models.

With measured ratios of He II to H I column densities, $\eta = N$(He II)/N(H I), we

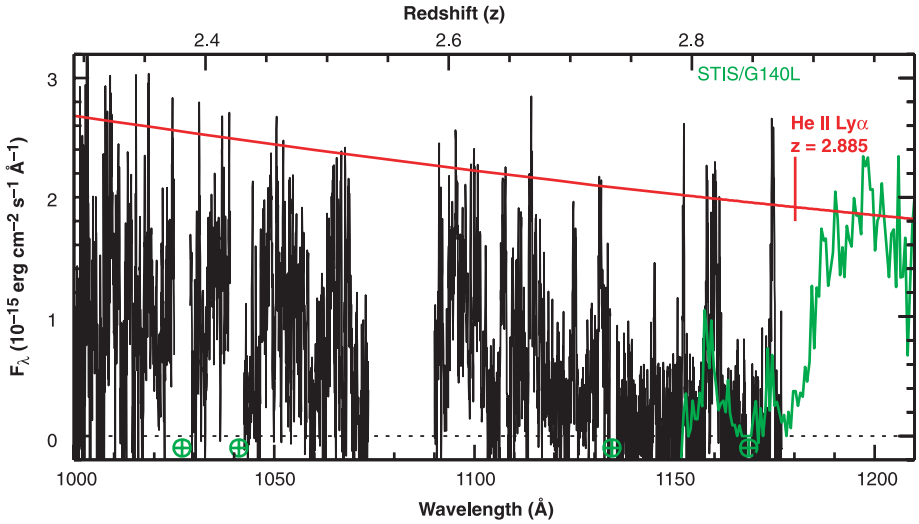

Fig. 1. FUSE spectrum of HE2347-4342 (binned to 0.05 Å pixels) is shown in black. Bins at the peak fluxes have a signal-to-noise ratio of ~7. A portion of the contemporaneous STIS spectrum is shown in green. The red line is the extrapolation of the power law plus extinction of $E(B-V) =$ 0.014 fitted to the STIS spectrum. The position of He II Lyα at the redshift of HE2347-4342 is marked. Gaps in the FUSE spectrum due to excised terrestrial airglow lines are marked with green ⊕. The broad gap from 1072 to 1089 Å is due to gaps between the FUSE detector segments.

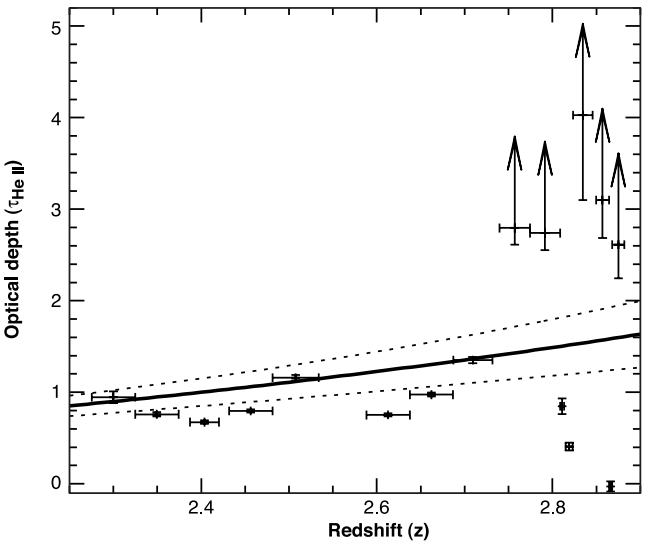

Fig. 2. The He II opacity $\tau_{\mathrm{He\ II}}$ in coarse 5 to 15 Å bins is shown as a function of redshift. The solid curve is the theoretical prediction for the opacity assuming line blanketing only (*21*). The dashed curves indicate the 1σ extent of variations in the opacity anticipated due to ionization fluctuations. At redshifts below $z = 2.72$, where the reionization of He II in the IGM appears to be complete, the model matches well the observed opacity, its trend to lower values at lower redshift, and the fluctuations about the mean.

can infer the shape of the ionizing spectrum illuminating the absorbing gas. Because our data include both measured values and lower limits (Fig. 4) (for He II Lyα features with no H I Lyα counterparts), we use the Kaplan-Meier estimator for censored data (*35*) to derive a mean value $\langle \log \eta \rangle = 1.89 \pm 0.04$ for the full data set. Models of an IGM photoionized by the integrated light from quasars propagated through the IGM (*21, 36*) predict values of $\eta = 30$ to 100 for quasar spectra with spectral indices $\alpha_q = 1.5$ to 2.1 ($f_\nu \propto \nu^{-\alpha_q}$). Intrinsic spectral indices for quasars (as measured down to a rest wavelength of ~350 Å) lie in this range (*37*). Thus, most of the observed absorption features are consistent with photoionization by quasar radiation. However, about 40% of the absorbers have $\eta > 100$, indicating that localized regions of the IGM are photoionized by softer spectra. This might be heavily filtered quasar radiation (in regions where the reionization of He II is not yet complete) or stellar radiation from ongoing star formation (*21*).

There are fluctuations in η on the scale of individual spectral features (Fig. 4), which implies that the ionizing radiation field is not uniform. Local radiation sources (which may be either quasars or star-forming galaxies) probably affect η and the local opacity of the IGM. This characteristic is most evident at high z in the low-opacity "windows" first seen in HST spectra of HE2347-4342 (*22, 23*), but it persists to lower redshift where the IGM is less opaque.

By resolving the He II Lyα absorption in the IGM using FUSE, we are able to see structure in the universe that extends into the lowest density regions. The presence of He II absorption with no H I counterparts is con-

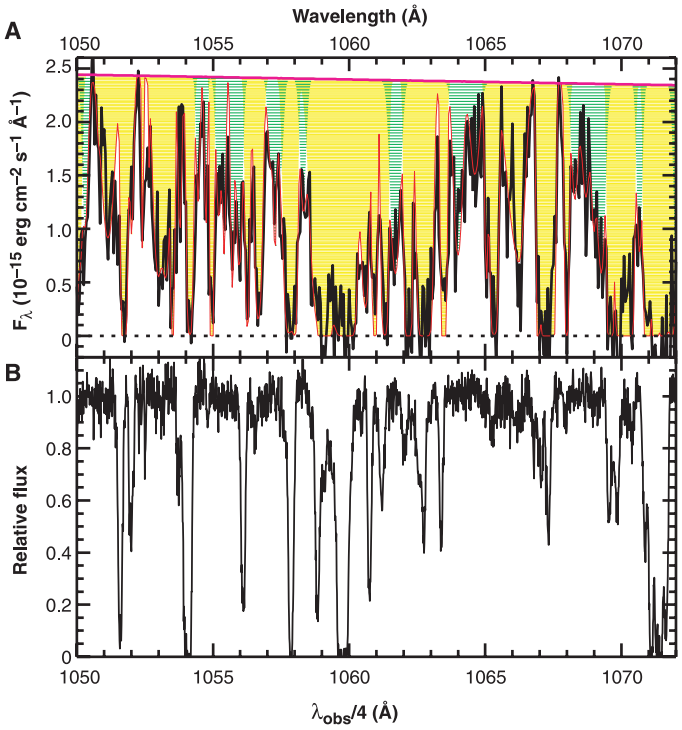

Fig. 3. (**A**) The black line is a portion of the FUSE spectrum of HE2347-4342. The smooth red curve across the top is the extrapolated continuum. The magenta line overlaying the spectral data in black is the model described in the text. The area shaded in yellow shows the fraction of the He II opacity due to absorption features that correspond to H I absorption lines identified in the Keck spectrum (*32*). The area shaded in green shows the fraction of the opacity due to additional He II absorption features that have no H I counterparts in the Keck spectrum. (**B**) The normalized Keck spectrum (*32*). Note the direct correspondence between the wavelengths of H I lines in the Keck spectrum and He II absorption features in the FUSE spectrum.

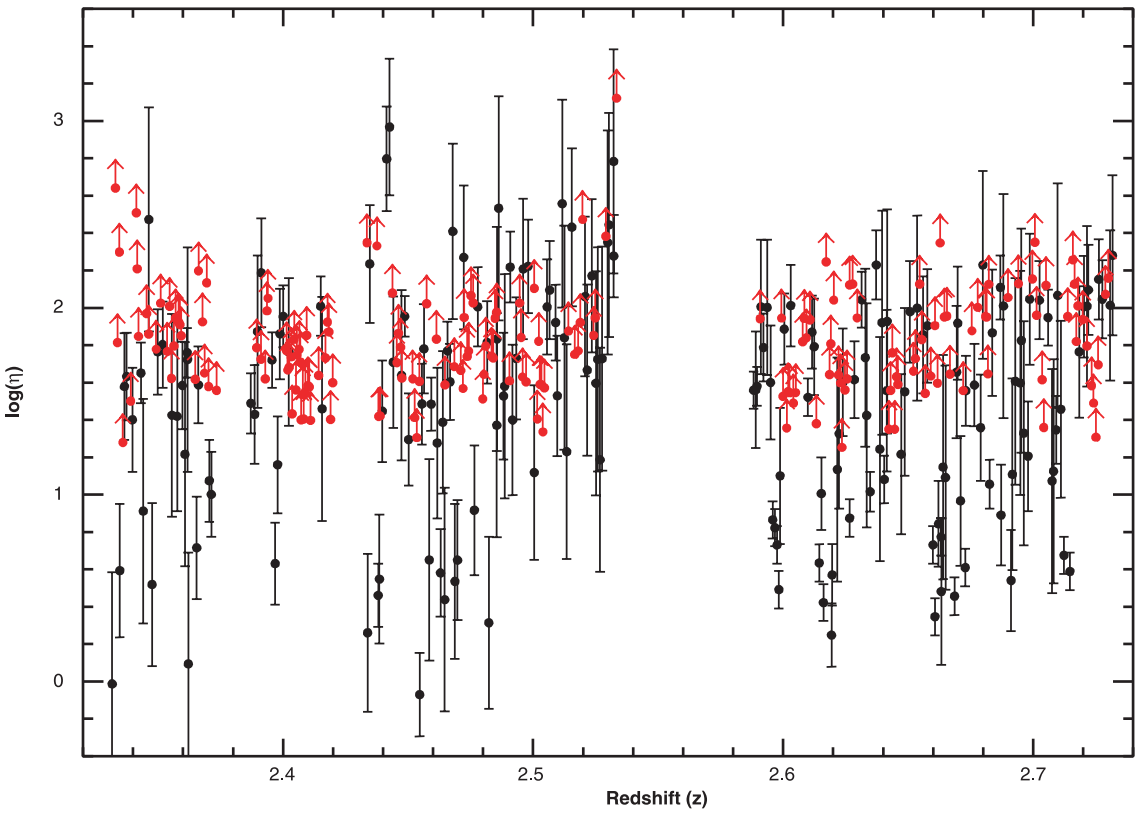

Fig. 4. The logarithm of the He II to H I column density ratio $\eta = N$(He II)/N(H I) versus redshift for measured absorption features in the FUSE spectrum. The black points with error bars have measured column densities for both He II (from FUSE) and H I (from Keck). The red points are lower limits computed using the He II column density measured from the FUSE spectrum and an upper limit of $10^{12.3}$ cm^{-2} for H I absorption lines in the Keck spectrum. A Spearman rank correlation coefficient of 0.05 indicates that there is no significant trend with redshift. The mean value, $\langle \log \eta \rangle = 1.89$, is consistent with photoionization of the IGM by integrated quasar light (*21, 36*). However, one can see significant fluctuations in η that indicate that the ionizing radiation field is not uniform. Values of $\eta > 100$ indicate regions photoionized by either heavily filtered quasar radiation or bursts of star formation.

sistent with hydrodynamical models that predict density fluctuations due to gravitational instabilities on all scales, from the high-density peaks that form galaxies to the distribution of gas in low-density voids (*9–16, 19, 20*). Observation of He II Lyα absorption is the best method to study these regions, and future observations of additional bright quasars with FUSE should provide essential information on the cosmic variance in the structures we see along different lines of sight.

References and Notes

1. J. Gunn, B. Peterson, *Astrophys. J.* **142**, 1633 (1965).
2. R. Lynds, *Astrophys. J.* **164**, L73 (1971).
3. P. Jakobsen *et al*., *Astrophys. J.* **417**, 528 (1993).
4. P. Jakobsen *et al*., *Nature* **370**, 35 (1994).
5. A. Songaila, E. M. Hu, L. L. Cowie, *Nature* **375**, 124 (1995).
6. A. F. Davidsen, G. A. Kriss, W. Zheng, *Nature* **380**, 47 (1996).
7. W. Zheng, A. F. Davidsen, G. A. Kriss, *Astron. J.* **115**, 391 (1998).
8. S. R. Heap *et al*., *Astrophys. J.* **534**, 69 (2000).
9. R. Cen, J. Miralda-Escudé, J. P. Ostriker, M. Rauch, *Astrophys. J.* **437**, L9 (1994).
10. Y. Zhang, P. Anninos, M. L. Norman, *Astrophys. J.* **453**, L57 (1995).
11. _____, A. Meiksin, *Astrophys. J.* **485**, 496 (1997).
12. L. Hernquist, N. Katz, D. H. Weinberg, J. Miralda-Escudé, *Astrophys. J.* **457**, L51 (1996).
13. J. Miralda-Escudé, R. Cen, J. P. Ostriker, M. Rauch, *Astrophys. J.* **471**, 582 (1996).
14. R. A. C. Croft, D. H. Weinberg, N. Katz, L. Hernquist, *Astrophys. J.* **488**, 532 (1997).
15. R. Cen, J. P. Ostriker, *Astrophys. J.* **514**, 1 (1999).
16. R. Davé, L. Hernquist, N. Katz, D. H. Weinberg, *Astrophys. J.* **511**, 521 (1999).
17. H. Bi, *Astrophys. J.* **405**, 479 (1993).
18. _____, J. Ge, L.-Z. Fang, *Astrophys. J.* **452**, 90 (1995).
19. H. Bi, A. F. Davidsen, *Astrophys. J.* **479**, 523 (1997).
20. L. Hui, N. Y. Gnedin, Y. Zhang, *Astrophys. J.* **486**, 599 (1997).
21. M. A. Fardal, M. L. Giroux, J. M. Shull, *Astron. J.* **115**, 2206 (1998).
22. D. Reimers *et al*., *Astron. Astrophys.* **327**, 890 (1997).
23. A. Smette *et al*., *Astrophys. J.*, in press (available at http://xxx.lanl.gov/abs/astro-ph/0012193).
24. FUSE covers the wavelength range 912 to 1187 Å with four separate optical channels (*38, 39*). Each channel consists of an off-axis paraboloidal mirror feeding a prime-focus Rowland circle spectrograph. The dispersed light is focused on two 2D photon-counting microchannel-plate detectors with KBr photocathodes that record the time, position, and pulse height of each photon event. Each detector is split into two segments with a small gap between them. Two channels use LiF-coated optics to cover the band 1000 to 1187 Å; the other two channels use SiC coatings to provide short-wavelength coverage down to 912 Å.
25. Because the count rate in a 50,000-s observation in June 2000 was lower than the typical background rate, we chose the dates of these observations to maximize the exposure time during orbital night, the part of the orbit when FUSE is in Earth's shadow. This minimizes the background contribution due to scattered geocoronal Lyα.
26. To obtain the lowest background rate possible, we used only orbital night observations, filtered the high-background "bursts" (*39*) from the data, and used only events with pulse heights in the range 4 to 16. This reduces noise due to the low-pulse-height events that arise from internal detector background rather than from real photons.
27. J. Cardelli, G. Clayton, J. Mathis, *Astrophys. J.* **345**, 245 (1989).
28. D. J. Schlegel, D. P. Finkbeiner, M. Davis, *Astrophys. J.* **500**, 525 (1998).
29. Although the mean opacity is tightly constrained, we note that there is a large dispersion of 0.9 about this value.
30. G. A. Kriss, in *Astronomical Data Analysis Software and Systems III*, D. R. Crabtree, R. J. Hanisch, J. Barnes, Eds., *ASP Conf. Series 61* (Astronomical Society of the Pacific, San Francisco, 1994), p. 437.
31. For the low extinction along this sight line, the interstellar absorption model contributes strong features only for Si II λ1020, Lyβ λ1025, C II λ1036, O I λ1039, Ar I λλ1048, 1066, and no H_2 absorption. Along similar high-latitude sight lines observed with FUSE, the column density in H_2 is on the order of a few $\times 10^{15}$ cm^{-2} [J. M. Shull *et al*., *Astrophys. J.* **538**, L73 (2000)]. The average opacity produced by such a column density amounts to <4% from 1000 to 1110 Å.
32. A. Songaila, *Astron. J.* **115**, 2184 (1998).
33. W. H. Press, G. B. Rybicki, *Astrophys. J.* **418**, 585 (1993).
34. E. M. Hu, T.-S. Kim, L. L. Cowie, A. Songaila, M. Rauch, *Astron. J.* **110**, 1526 (1995).
35. E. D. Feigelson, P. I. Nelson, *Astrophys. J.* **293**, 192 (1985).
36. P. Madau, F. Haardt, M. J. Rees, *Astrophys. J.* **514**, 648 (1999).
37. W. Zheng, G. A. Kriss, R. C. Telfer, J. P. Grimes, A. F. Davidsen, *Astrophys. J.* **475**, 469 (1997).
38. H. W. Moos *et al*., *Astrophys. J.* **538**, L1 (2000).
39. D. Sahnow *et al*., *Astrophys. J.* **538**, L7 (2000).

40. We sadly report that Arthur F. Davidsen, one of our key team members and a pioneer in ultraviolet observations of the IGM, passed away on 19 July 2001. This work is based on data obtained for the Guaranteed Time Team by the NASA-CNES-CSA FUSE mission operated by Johns Hopkins University. Financial support to U.S. participants has been provided by NASA contract NAS5-32985 and by NASA LTSA grant NAG5-7262 to the University of Colorado. A portion of this work is based on observations with the NASA/ESA Hubble Space Telescope, obtained at the Space Telescope Science Institute, which is operated by the Association of Universities for Research in Astronomy Inc. under NASA contract NAS5-26555. These observations are associated with proposal ID 8875. We thank B. Roberts for his efforts in planning and scheduling the successful FUSE observations, and J. Kim for her help in analyzing the STIS data.

21 May 2001; accepted 3 July 2001

No Supermassive Black Hole in M33?

David Merritt,* Laura Ferrarese, Charles L. Joseph

We observed the nucleus of M33, the third-brightest galaxy in the Local Group, with the Space Telescope Imaging Spectrograph at a resolution at least a factor of 10 higher than previously obtained. Rather than the steep rise expected within the radius of gravitational influence of a supermassive black hole, the random stellar velocities showed a decrease within a parsec of the center of the galaxy. The implied upper limit on the mass of the central black hole is only 3000 solar masses, about three orders of magnitude lower than the dynamically inferred mass of any other supermassive black hole. Detecting black holes of only a few thousand solar masses is observationally challenging, but it is critical to establish how supermassive black holes relate to their host galaxies, and which mechanisms influence the formation and evolution of both.

At a distance of 850 kiloparsecs (kpc) from Earth, M33 is classified (*1*) as a late-type ScII-III spiral, consistent with its almost nonexistent bulge (*2, 3*). The nucleus of M33 is very compact, reaching a stellar central mass density of several million solar masses per cubic parsec (*4, 5*), larger than that of any globular cluster. Although such high nuclear densities might be expected in the presence of a supermassive black hole (SMBH) (*6*), ground-based data show no evidence for a central rise in stellar velocities that would indicate the presence of a compact massive object in the nucleus (*4*).

M33 was observed on 12 February 1999 with the Space Telescope Imaging Spectrograph (STIS) on the Hubble Space Telescope (HST). Three sets of two long-slit spectra each, for a total exposure time of 7380 s, were obtained using the G750M grating centered on the CaII absorption triplet near 8561 Å (1 Å corresponds to 10^{-10} m), covering 19.6 km s^{-1} pixel^{-1}. The pixel scale is 0″.05 with a spatial resolution of 0″.115 at 8561 Å. While the two spectra in each set were obtained at the same position to facilitate removal of cosmic ray events, the nucleus was moved along the slit by 0″.216 between each consecutive set. This dithering procedure allows for optimal correction of residual variations in the detector sensitivity as well as identification and removal of malfunctioning pixels. The calibration steps followed the standard procedure (*7*) adopted for STIS observations of the nucleus of M32.

The observed spectrum (Fig. 1) at every resolution element is the convolution of the spectra of individual stars with the line-of-sight velocity distribution (LOSVD) of the stellar ensemble; the latter contains information about the mean and random velocities of stars in the nucleus, projected along the line of sight through the galaxy. We adopted as a typical stellar spectrum that of the K0 III

Department of Physics and Astronomy, Rutgers University, New Brunswick, NJ 08854, USA.

*To whom correspondence should be addressed. E-mail: merritt@physics.rutgers.edu